Earth and Planetary Science Letters, 118 (1993) 213–234
Elsevier Science Publishers B.V., Amsterdam

[PT]

High-temperature metamorphism in a major strike-slip shear zone: the Ailao Shan–Red River, People's Republic of China

Philippe H. Leloup [a] and Jean-Robert Kienast [b]

[a] *Laboratoire de tectonique, Institut de Physique du Globe de Paris, 4 place Jussieu, 75252 Paris Cedex 05, France*
[b] *Laboratoire de pétrologie, Université Paris VII, 4 place Jussieu, 75252 Paris Cedex 05, France*

Received June 29, 1992; revision accepted April 30, 1993

ABSTRACT

Petrographic and thermobarometric analysis provides constraints on the *PT* path of the mylonitic gneisses of the left-lateral Ailao Shan–Red River shear zone which has accommodated the lateral extrusion of Indochina during the Tertiary. Two different paragenesis, P1 and P2, are coeval with this deformation and correspond respectively to the amphibolite and greenschist facies. Microprobe analysis reveals that P1 garnets bear a chemical zonation from core to rim. This zonation indicates a temperature increase during garnet growth. Conditions of formation of garnet rims (P1b), which are estimated using biotite–garnet and plagioclase–garnet thermobarometers, are close to the granitic solidus (710 ± 70°C and 4.5 ± 1.5 kbar). P2 conditions are estimated to be approximately 500°C and < 3.8 kbar. Both P1b and P2 conditions correspond to much higher temperatures than expected for their depths in the continental crust, suggesting a perturbed geothermal gradient during strike-slip deformation along the Ailao Shan–Red River shear zone. Thermochronology results suggest that cooling between P1b and P2 was fast (≈ 100°C/Ma) and may have been associated with significant uplift. Uplift during the left-lateral shearing may have resulted from a slight reverse or, more probably normal, component of movement along the strike-slip fault. A simple numerical model suggests that the high temperatures in the shear zone at the time of deformation may be explained by shear heating in the more competent upper mantle and by advection of this heat along the shear zone by ascent of magmas and/or fluids. In this hypothesis, the medium-pressure and temperature schists bounding the mylonitic gneisses to the southwest previously interpreted as resulting from collision-related metamorphism result instead from 'contact' metamorphism of the shear zone at mid-crustal depths.

1. Introduction

Most tectonic events within continents involve an increase in the crustal geothermal gradient. For example, continental collision often results in large-scale thickening, causing regional metamorphism. Strike-slip faulting does not induce large vertical movement and is usually not considered to be responsible for significant metamorphism. Continental strike-slip shear zones are often found within orogenic belts where high-grade metamorphism is widespread. This metamorphism is now well documented and seems to be mainly due to crustal thickening. However, it is more difficult to evaluate the metamorphism, if any, that is due to strike-slip faulting. In this paper we investigate high-grade metamorphism along a strike-slip shear zone in an area where continental crust has not been significantly thickened and where the metamorphism is restricted to the shear zone.

The Red River fault zone (RRFZ) is a Tertiary left-lateral continental strike-slip fault that allowed the southeasterly escape of the Indochina block in response to the India–Eurasia collision (Fig. 1a) [1,2]. Intense left-lateral ductile deformation is observed in four metamorphic massifs stretching for more than 900 km from northwest Yunnan in PRC to Vietnam. These massifs define the Ailao Shan–Red River shear zone [1,3,4]. Cenozoic left-lateral offset along this shear zone is probably greater than 500 km [1,4,5]. In this paper we present petrographic and thermobarometric analyses of mylonitic rocks from

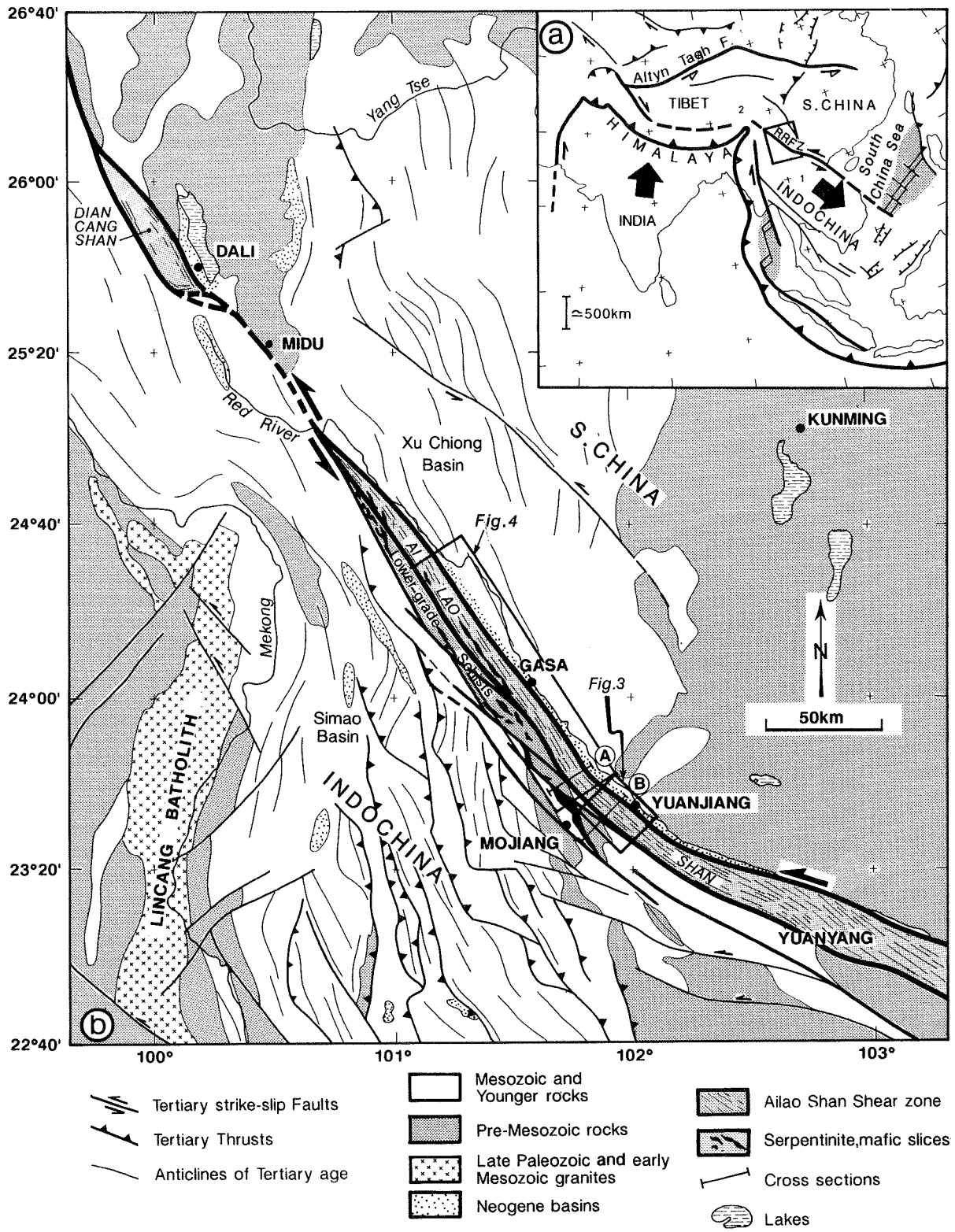

Fig. 1. (a) Schematic map of major Cenozoic fault zones in Asia. Inset corresponds to (b). *RRFZ* = Red River fault zone. (b) Map of post-Cretaceous tectonics of Yunnan province. Boxes correspond to Figs. 3 and 4; A and B correspond to cross sections of Fig. 2. Modified from [1].

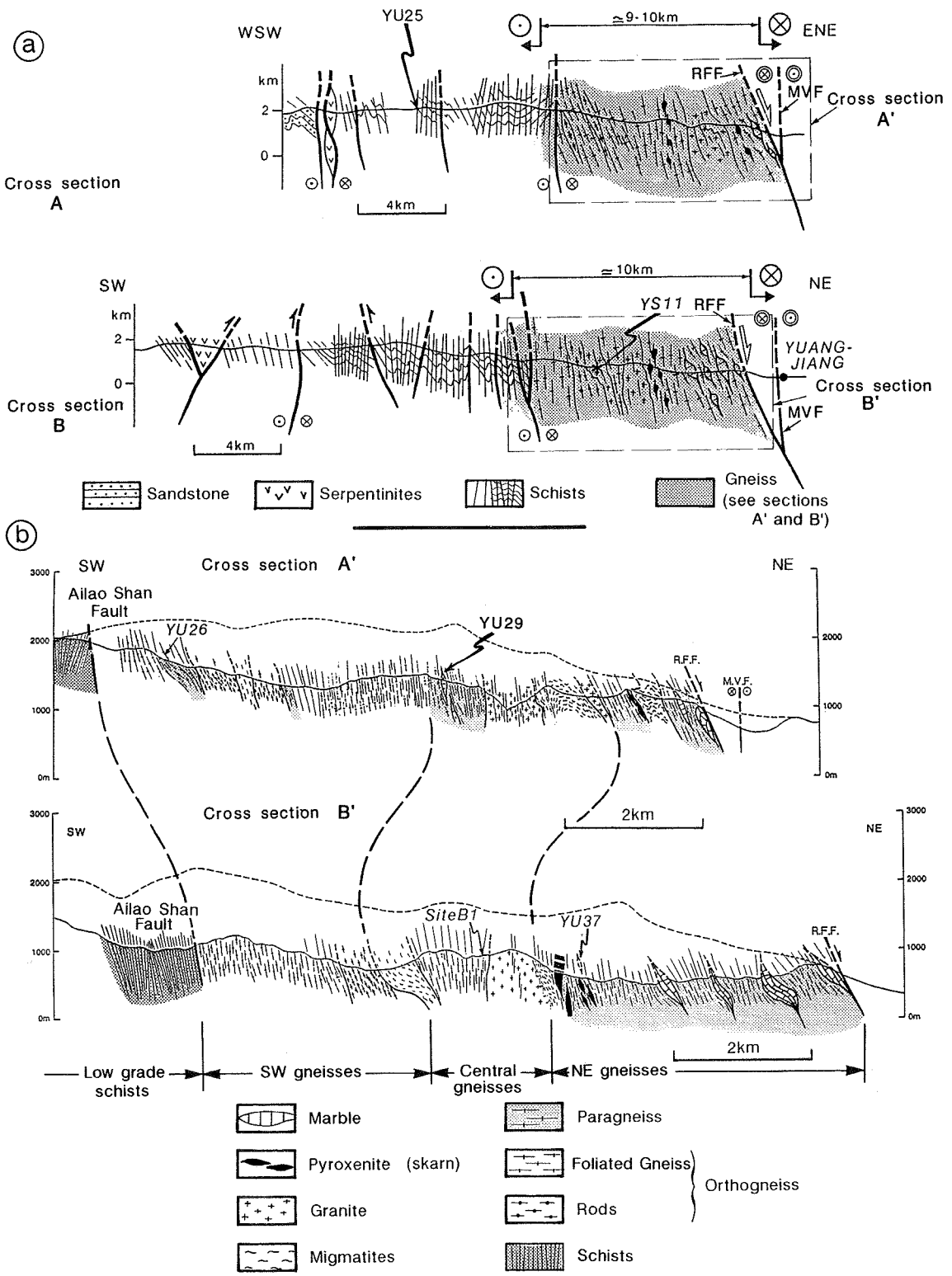

g. 2. Cross sections through the Ailao Shan metamorphic belt (location in Fig. 1b). (a) General cross sections. (b) detailed cross sections through gneissose units. *RFF* = Range Front fault (mainly normal); *MVF* = Mid-Valley fault (purely strike-slip).

the Ailao Shan massif deformed during this left-lateral shearing. As this deformation took place at very high temperatures and moderate depth we investigate possible heat sources that include shear heating. The evaluation of the importance of shear heating in continental lithosphere is critical as it is an appealing mechanism for explaining large-scale strain softening and deformation localization.

2. Geological setting

2.1 Regional geology

The Red River fault zone may be followed for over 1000 km from Tibet to the South China Sea, separating the Yangtze platform or South China block to the north and the Indochina or Sundaland block to the south (Fig. 1a) [e.g., 1,6]. The

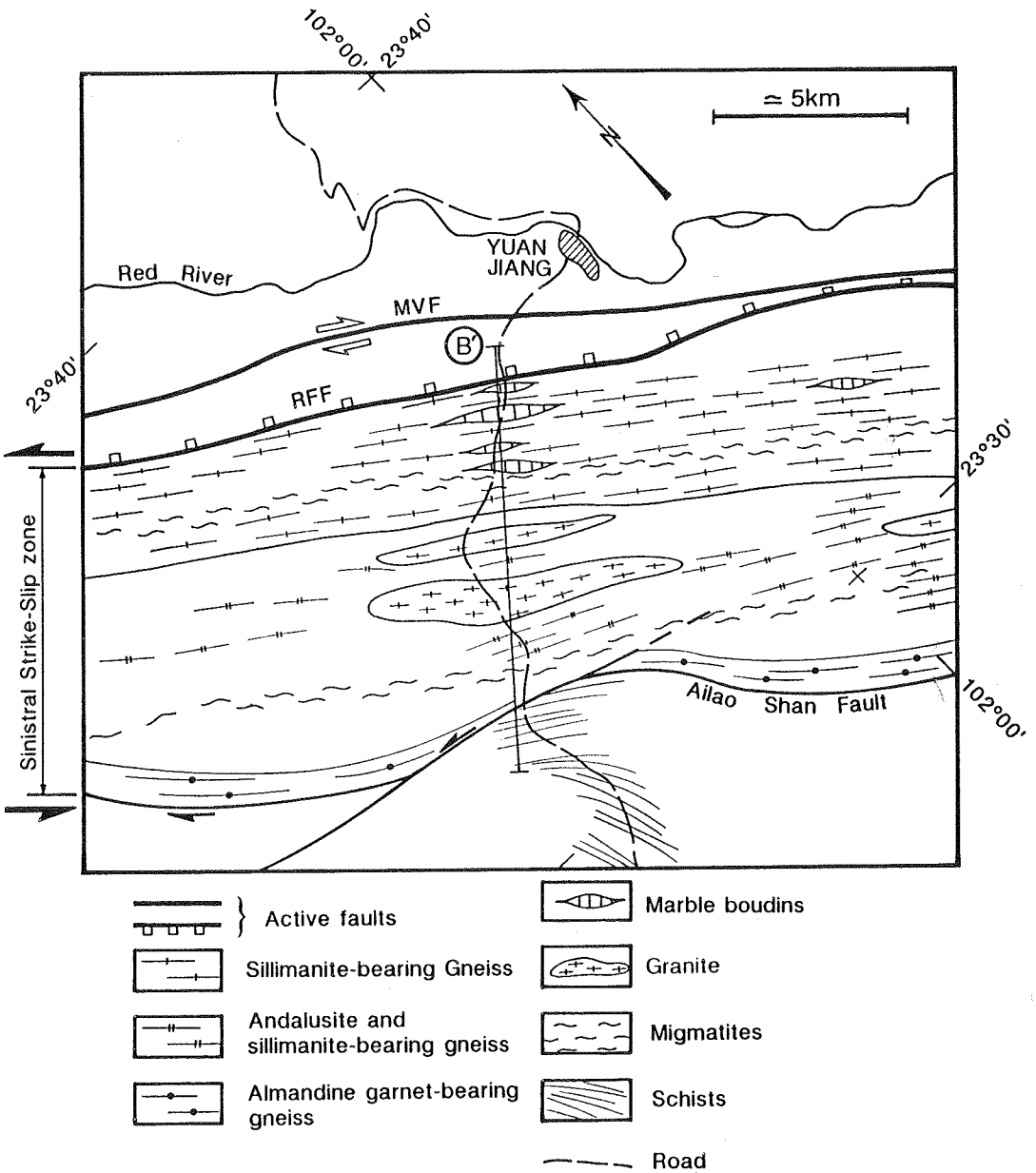

Fig. 3. Simplified metamorphic map of the Ailao Shan massif southwest of Yuanjiang (box in Fig. 1b). From the 1:200,000 geological map, our observations along the Yuanjiang–Mojiang road (cross section B) and an unpublished Chinese document.

Red River fault system is presently active, with right-lateral slip combined with normal throw [7,8]. This active fault system follows the edge of narrow gneissose belts: the Ailao Shan, Diancang Shan and Xuelong Shan ranges in Yunnan province (Fig. 1b) and the Dai Nuy Con Voi in Vietnam.

Both sides of the Red River fault zone correspond to essentially unmetamorphosed sediments. To the north, the Yangtze platform is characterized by a nearly continuous sedimentary succession ranging in age from Devonian to Eocene. Outcrops of the Yangtze platform basement are very scarce. South of the Red River fault zone, the Simao sedimentary basin, which ranges in age from Silurian to Eocene, is bounded to the southwest by the large Permian S-type Lincang granitic batholith [9,10]. This large granitic body intruded metamorphic rocks of unknown age (Fig. 1b) [9]. On both sides of the Red River fault zone, Upper Triassic to Eocene continental red sandstone is affected by folds with a steep axial plane cleavage striking NNW–SSE, indicating a nearly E–W Cenozoic compression [4] (Fig. 1b). Corresponding shortening is moderate (less than 25%) [4]. The Moho depth is estimated at ≈ 40 km north of the fault zone and ≈ 30 km south of it [11].

2.2 Tertiary left-lateral movement along the Ailao Shan–Red River shear zone

The presence of ultramafic rocks surrounded by low-grade schists on the southwest border of the Ailao Shan gneissose belt has led many authors to interpret these gneisses as a slab of the Precambrian basement of the Yangtze platform [e.g., 12,13] thrust to the southwest onto blueschists and ophiolites during a continental collision [e.g., 12,14]. Many authors believe that this collision occurred during the Triassic (the 'Indosinian orogeny') [e.g., 6,15,16,17] and have interpreted the Red River fault zone as a suture zone.

However, recent tectonic and geochronological studies show that the metamorphic massifs of the Red River fault zone correspond to a major Tertiary left-lateral shear zone, the Ailao Shan–Red River shear zone [e.g., 1,2]. In the 10–20 km wide gneissose cores of the Ailao Shan, Diancang Shan and Xue Long Shan, most rock types are mylonitic and foliation is generally steep and always parallel to the strike of the belt (Figs. 2 and 3) [1–4]. The stretching lineation is well developed and everywhere subhorizontal. There is ample unambiguous evidence for non-coaxial deformation. Various kinematic indicators consistently indicate a left-lateral sense of shear [1–4]. In the Ailao Shan, monazite and xenotime U/Pb ages from late syntectonic leucogranitic veins parallel to the foliation and affected by left-lateral shear cluster at 23 ± 0.2 Ma [2]. This age pre-dates the late increments of left-lateral ductile shear. Estimates of left-lateral offset of geological features across the shear zone range between 300 and 740 km [4,5]. The kinematics of the opening of the South China Sea during the Oligocene through to the middle Miocene (32–16 Ma BP), as deduced from magnetic anomalies, is compatible with a left-lateral movement (with a slight oblique component) of 540 km along the RRFZ [18,19]. These kinematic data support the interpretation that the South China Sea evolved as a pull-apart basin at the southeastern termination of the Ailao Shan–Red River shear zone (Fig. 1a) and indicate slip rates of between 5.5 and 3.3 cm/yr along this fault [18,19].

In this paper we discuss the petrology of the largest of the metamorphic massifs of this shear zone, the Ailao Shan (Fig. 1b)

3. Petrology of the Ailao Shan belt

The Ailao Shan is a long (≈ 400 km) and narrow (on average 20 km) metamorphic belt bounded to the northeast by the active Red River fault. Our description of the petrology of the central part of the Ailao Shan massif is based on our fieldwork and data from 1 : 200,000 geological maps (Figs. 2 and 3). The Ailao Shan massif is composed of two main parallel units: high-grade gneisses to the northeast and schists containing ultramafic rocks to the southwest (Fig. 1b).

3.1 Ailao Shan high-grade gneisses

South of the Yangtze platform, the NNW–SSE steep cleavage affecting the Mesozoic cover rocks becomes progressively stronger and nearly parallel to the Red River fault zone. Near Yuanjiang

(Fig. 1b), on the northern bank of the Red River, the Mesozoic rocks are metamorphosed to a very low grade. South of the Red River, the northern boundary of the Ailao Shan high-grade metamorphic massif comprises one of the two branches of the active Red River fault—the Range Front fault (RFF), which is clearly visible in the geomorphology [8] (Figs. 2 and 3). The juxtaposition of high-grade gneisses and very low grade metamorphic rocks seems to be partly due to the recent uplift of the gneisses along this normal fault [1,3,4,20]. The elongate high-grade meta-

paragenesis 1 (P1) Minerals stable during ductile deformation Amphibolite facies	paragenesis 2 (P2) Minerals filling cracks or pressure shadows Greenschist facies
YU 15 (site E1)	
Quartz (ribbon) Feldspar porphyroblasts Schistosity underlined by biotite	Chlorite+Biotite
YU 16 (site E1)	
Quartz (ribbon) Feldspar porphyroblasts. Schistosity underlined by biotite	Chlorite+Biotite
YU 19 (site E4)	
Quartz (ribbons) Feldspar porphyroblasts Plagioclase porphyroblasts Garnets Schistosity underlined by biotites lineation underlined by sillimanites	Chlorite+Biotite Calcite Chlorite+Muscovite Muscovite+Biotite
YU 20 (site E4)	
Quartz (ribbon) Feldspar porphyroblasts Plagioclase porphyroblasts Garnets Schistosity underlined by biotite lineation underlined by sillimanites *Barometer plagioclase-garnet* *Thermometer biotite-garnet*	Chlorite+Biotite Calcite Chlorite+Muscovite Muscovite+Biotite
YU21 (site E5)	
Quartz (ribbon) Feldspar porphyroblasts (Plagioclase porphyroblasts) Garnets Schistosity underlined by biotites lineation underlined by sillimanites	Chlorite+Muscovite Biotite+Chlorite+Muscovite Muscovite *Geothermobarometer* *Biotite+Chlorite+Muscovite*
YU24 (site E6)	
Quartz (ribbon) Feldspar porphyroblasts (Plagioclase porphyroblasts) Garnets Schistosity underlined by biotites lineation underlined by sillimanites *Thermometer biotite-garnet*	Chlorite+Biotite Chlorite+Biotite

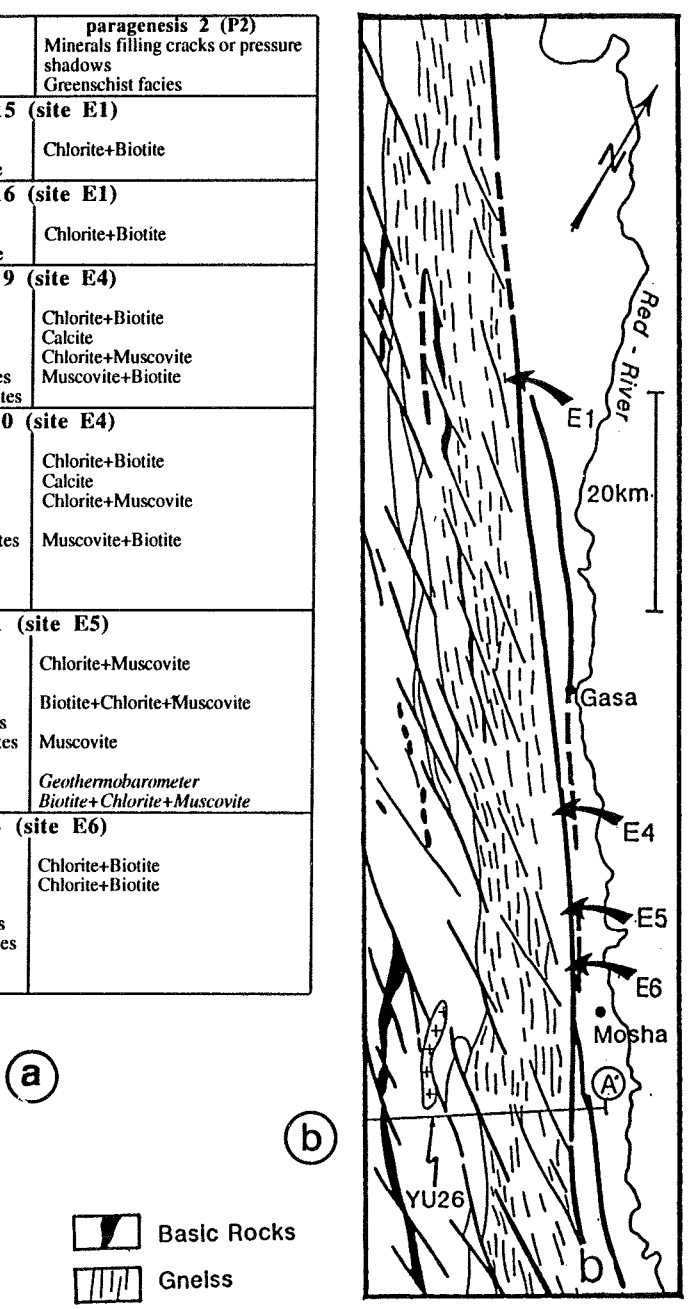

Fig. 4. Location of sampling and mineral parageneses on the northeastern border of the Ailao Shan massif (samples YU15, 16, 19, 20, 21 and 24).

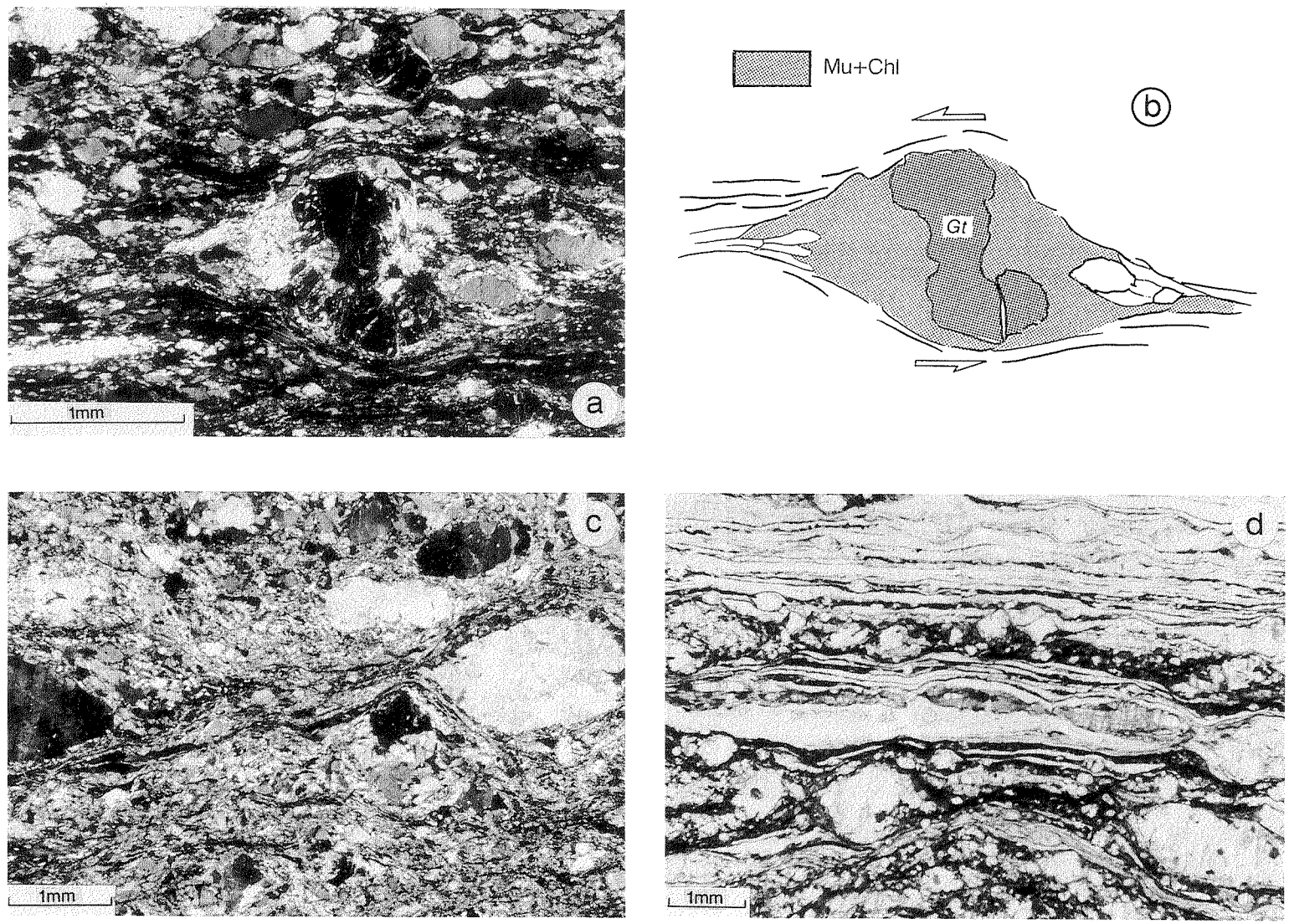

Fig. 5. Thin section microphotographs of samples from the northeastern border of the Ailao Shan massif showing the amphibolite facies paragenesis (P1) and the greenschist facies paragenesis (P2). Thin sections parallel to lineation and perpendicular to schistosity (≈ horizontal plane). (a and b) Crossed nicols section and interpretative sketch of a garnet (P1) that has developed asymmetric pressure shadows filled with chlorite and muscovite (P2). The shape of the retrograde pressure shadows indicates a left-lateral sense of shear. Sample YU19 (site E4, Fig. 4). (c) Left-lateral shear plane marked by biotites (P1). (d) Biotite outlining the schistosity and stretched sillimanites outlining the mineral lineation (P1).

morphic core of the Ailao Shan, which coincides with a topographic high, is composed of an 8–10 km wide zone of mylonitic gneisses, migmatites and granitic pods, forming slabs subparallel to the trend of the belt that dip steeply towards the northeast (Fig. 2). Compositional layering and metamorphic mineral zones are parallel to the prominent mylonitic foliation (Figs. 2 and 3). High-grade gneisses are separated toward the southwest from the schists by the Ailao Shan fault (Figs. 2 and 3). Three units may be distinguished within the Ailao Shan gneisses, the northeastern unit, the central and the southwestern (Fig. 2).

3.1.1 Northeastern Ailao Shan gneisses

The northeastern Ailao Shan gneisses correspond to thinly banded mylonitic paragneisses that contain stretched amphibolite layers, deformed leucocratic veins, migmatitic zones, garnet-pyroxenite boudins, and large-scale ($\approx$ 100 m wide) white marble boudins (Figs. 2b and 3). Between amphibolite layers, these paragneisses are essentially of metapelitic composition and exhibit two successive parageneses. The first (P1) corresponds to quartz + plagioclase $\pm$ K-feldspar + biotite $\pm$ garnet $\pm$ sillimanite (Figs. 4, 5c and 5d). Sillimanite is stable at temperatures higher than 470°C [21], and its association with biotite

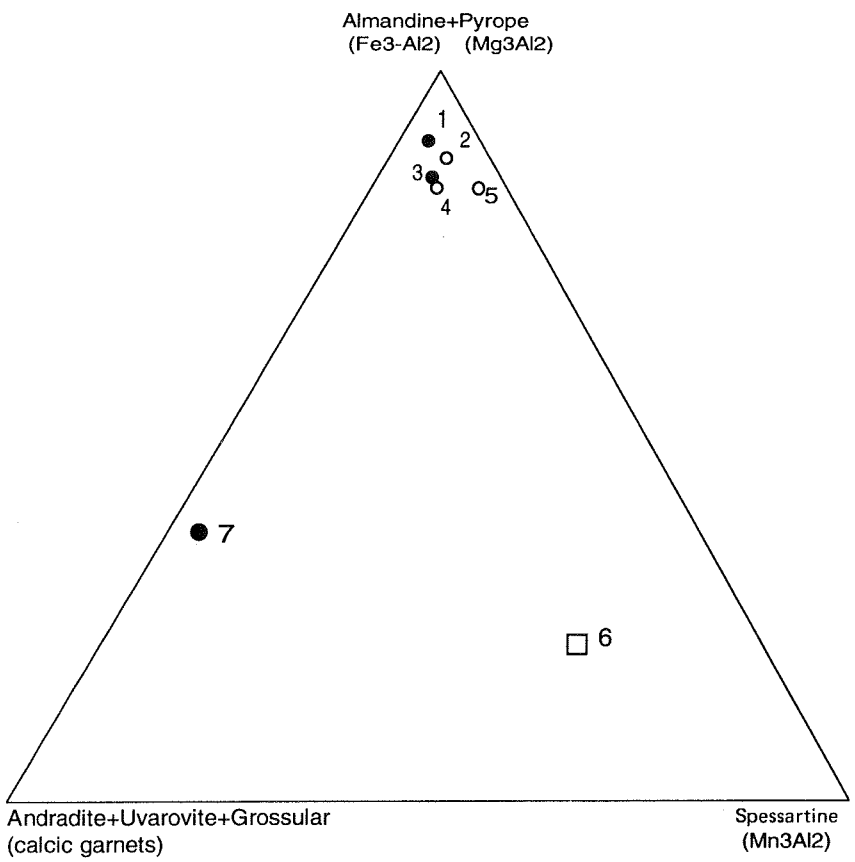

Fig. 6. Comparison of garnet chemical composition in samples YU20, 21, 24, 26 and 37. See Figs. 2b and 4 for sample locations. Data from electron microprobe measurements. Garnets of samples YU20, 21 and 24 have very comparable compositions and are high grade (P1). P1a and P1b corresponds to measurement in the core and near the rim of the garnets respectively (see Figs. 7, 9 and 10 and text). *1* = P1a garnet from sample YU20 (average of spots 1, 2, 3, 4, 6, 8 and 9); *2* = P1b garnet from sample YU20 (average of spots 12, 13, 14, 33 and 34); *3* = P1a garnet from sample YU24 (average of spots 53 and 46); *4* = P1b garnet from sample YU24, *5* = P1 garnets of sample YU21 (average of spots 1, 2, 3 and 4); *6* = garnets of sample YU26; *7* = garnets of sample YU37. YU26 garnets have a higher Mn content and correspond to lower grade conditions (P2). YU37 garnets are rich in Ca (59% calcic garnet). Almandine = $Fe_3Al_2Si_3O_{12}$; pyrope = $Mg_3Al_2Si_3O_{12}$; spessartine = $Mn_3Al_2Si_3O_{12}$; grossular = $Ca_3Al_2Si_3O_{12}$; andradite = $Ca_3Fe_2Si_3O_{12}$; uvarovite = $Ca_3Cr_2Si_3O_{12}$.

and garnet indicates that P1 corresponds to amphibolite facies metamorphism. Biotites outline the mylonitic foliation as well as small-scale left-lateral shear planes (C or C' planes) (Figs. 5c and d). Sillimanite crystals are always parallel to the stretching lineation, suggesting growth during deformation (Fig. 5d). These observations indicate that P1 is coeval with the left-lateral deformation. A second metamorphic mineral assemblage appears in cracks and pressure shadows on P1 porphyroblasts. This paragenesis is characterized by retrograde minerals typical of greenschist metamorphic facies (P2: chlorite + muscovite ± biotite) (Figs. 4 and 5). The stretching direction deduced from the cracks filled with P2 minerals is parallel to the P1 lineation. Asymmetry of pressure shadows filled with P2 minerals indicates a left-lateral sense of shear (Figs. 5a and b). P1 and P2 seem to have been both stable during the left-lateral deformation. Leucocratic layers have a granitic composition and contain quartz, perthite, plagioclase and biotite. Zircon, monazite and xenotime are present as accessory phases [2]. We will discuss later the timing of emplacement of these leucocratic layers.

Large garnet-pyroxenite boudins (Fig. 2) have been interpreted as parts of lower crust-derived eclogite [Zhong Dalai, pers. commun.]. A thin section of sample YU37 from one of these boudins (Fig. 2b) shows many green clinopyroxenes, some garnets and numerous quartz and carbonate grains. Garnets most often grow at the contact between carbonates and clinopyroxenes. Microprobe analyses of these clinopyroxenes indicate that they are not omphacite (the classical sodium-rich pyroxene within eclogite) but hedenbergite (wollastonite 49%, ferrosilite 43%, enstatite 8%). Garnets are very rich in Ca (andradite 50%, almandine 37%, grossularite 9%) (Fig. 6), and the carbonates are calcites. These compositions differ substantially from the classical composition of these minerals in eclogite, where garnet typically has high Fe-Mg and low Ca and the clinopyroxene is rich in Na. Sample YU37 is probably not an eclogite but rather its chemistry corresponds to that of an impure carbonate rock (leached marble or leached calc-silicate gneiss). The occurrence of large marble boudins nearby (less than 1 km away, Fig. 2) is consistent with this interpretation. All the metacarbonates, metapelites and amphibolite layers of the northeastern Ailao Shan gneisses could be the result of metamorphism of the Yangtze platform sedimentary cover (Devonian and Permian limestone, Permian basalt, Mesozoic sandstone and pelites) in the Ailao Shan–Red River shear zone.

3.1.2 Central Ailao Shan gneisses

In the central part of the massif, granitic bodies that parallel the structural trend are larger and more numerous than in the northeastern gneiss unit (Figs. 2 and 3). Some of these granitic bodies are almost 1 km thick. Like the leucocratic layers within the northeastern gneisses, these granites are rich in alkalis and incompatible elements and could be the result of partial melting of the crust in the shear zone.

3.1.3 Southwestern Ailao Shan gneisses

The southwestern part of the high-grade gneisses is mainly composed of orthogneisses. Some are augen gneiss which probably resulted from metamorphism and deformation of granites within the shear zone, while others are rich in quartzitic metavolcanic rocks. The latter may be the result of metamorphism of Triassic volcanic rocks which outcrop southwest of the Ailao Shan massif [9].

3.2 Schists and ultramafic rocks

On the southwestern side of the Ailao Shan fault, the width of the schist outcrop reaches ≈ 10 km in the central part of the belt (Figs. 1b and 2) [9]. These schists contain ultramafic rocks between the northern end of the Ailao Shan and the town of Mojiang (Fig. 1b) [9] which are interpreted to be ophiolites [e.g., 6,12,14,16]. They usually occur as long serpentinite bodies that have been involved in the sinistral strike-slip deformation [4]. Zhang Qi et al. [22] describe a complete section of these rocks, containing lherzolites, harzburgites, gabbros, diabases, basalts and radiolarites north of Mojiang. The surrounding schists have been interpreted as blueschists resulting from a low-temperature–medium pressure metamorphism coeval with ophiolite obduction [12]. However, Zhang Ru Yuhan et al. [23] have studied schists bearing blue amphiboles, chlorite, phengite, epidote and sphene from sec-

tion A near Maloutang (Fig. 1b), and they conclude that these blue amphiboles contain a winchite centre with a peripheral ring of actinolite from which they estimate *PT* conditions of 4 kbar and 170°C. Our own measurements on specimens from sample YU25 collected from the same area (Fig. 2a) indicate that the blue amphiboles are magnesio-riebeckite and tremolite [4]. These data show that, despite the presence of blue amphiboles, the occurrence of an episode of high pressure in the Ailao Shan is not demonstrated and the 'blueschists' may instead be greenschists.

4. Thermobarometric estimates on the Ailao Shan gneisses

To estimate pressure–temperature conditions of the two parageneses observed in the gneisses along the northeastern border of the Ailao Shan we have performed microprobe analyses on samples YU20, YU21, YU24 and YU26 (Figs. 2 and 4). Minerals were analyzed with an automated CAMEBAX microprobe at the *Centre CAMPARIS, Université Pierre et Marie Curie*, Paris. The operating voltage was 15 kV and the current was 20 mA. The counting time was 10 s and the standards used were a combination of oxides and natural silicates. All the microprobe data from this study are listed in [4] and may be obtained from the authors.

4.1 Estimation of the pressure–temperature conditions of the high-grade paragenesis (P1)

To estimate the pressure–temperature conditions of the high-grade paragenesis we used the biotite–garnet geothermometer [24,25] and the plagioclase–garnet geobarometer [26,27] on samples containing sillimanite (Fig. 4). The garnets of samples YU20, YU21 and YU24 are rich in Fe and Mg (on average, almandine $\approx$ 60% and pyrope $\approx$ 30%) (Fig. 6). Detailed microprobe analysis along sections of garnets from samples YU20 and YU24 yield small but significant zoning of the Mg, Fe and Mn content (Fig. 7). Garnet cores show generally lower concentrations of Fe and Mn and higher concentrations of Mg than rims (Fig. 7).

In sample YU20, the garnets are mostly almandine in composition, but the cores are more pyrope rich than the rims (Fig. 7a). In the rims the Fe/Mg ratio is higher and Fe/Mn ratio is lower (Fig. 7a). The composition of the plagioclase is more albitic in the matrix (Ab 54%, An 45%) than for those plagioclases present as inclusions in the garnet (Ab 50%, An 49%). These variations may be interpreted as resulting from progressive chemical re-equilibration of neighbouring minerals during changes of pressure and temperature. Garnet rims seem to be in equilibrium with the minerals forming the foliation and the lineation (e.g., biotite and sillimanite). The centre of the garnets has apparently retained a memory of previous equilibrium between the garnets and the minerals that are now included in them. On the basis of these observations, we distinguish two high-grade parageneses: paragenesis 1a (P1a), corresponding to garnet cores and mineral inclusions, and paragenesis 1b (P1b), corresponding to garnet rims and the minerals in the foliation. For P1a we applied the plagioclase–garnet geobarometer [27] for the data pairs Gt1–Pl18, Gt3–Pl19, Gt4–Pl20, Gt6–Pl21, Gt8–Pl22, Gt16–Pl23 and 24 (Figs. 7a and 8a). For P1b, we applied the plagioclase–garnet geobarometer [27] for the pairs Gt12–Pl27, Gt13–Pl29, Gt14–Pl30, Gt34–Pl28 and Gt33–Pl26, and the biotite–garnet geothermometer [25] to the data pairs Gt12–Biot35, Gt13–Biot37 and Gt14–Biot39 (Figs. 7a and 8b).

Similar chemical zoning is observed in the garnets of sample YU24. However, if the general evolution is similar, points in the cores of the garnet but close to biotite inclusions (e.g., spots 49 and 50) will have the same composition as those of the garnet rims (Fig. 7b). Our interpretation is that this variation is due to a partial re-equilibration of the chemical composition of the garnet near the biotite inclusions during the development of P1b. This re-equilibration seems less important for points in the garnet centre farther from the biotite inclusions (e.g., spots 46 and 53, Fig. 7) and thus we choose to apply the biotite–garnet thermometer [27] to the data pairs Gt53–Biot59 and Gt46–Biot56 for P1a and Gt54–Biot61 for P1b (Figs 7b and 8).

Figure 8 summarizes the P1a and P1b thermobarometer results. The *PT* conditions of P1a and P1b are estimated at the intersection between the

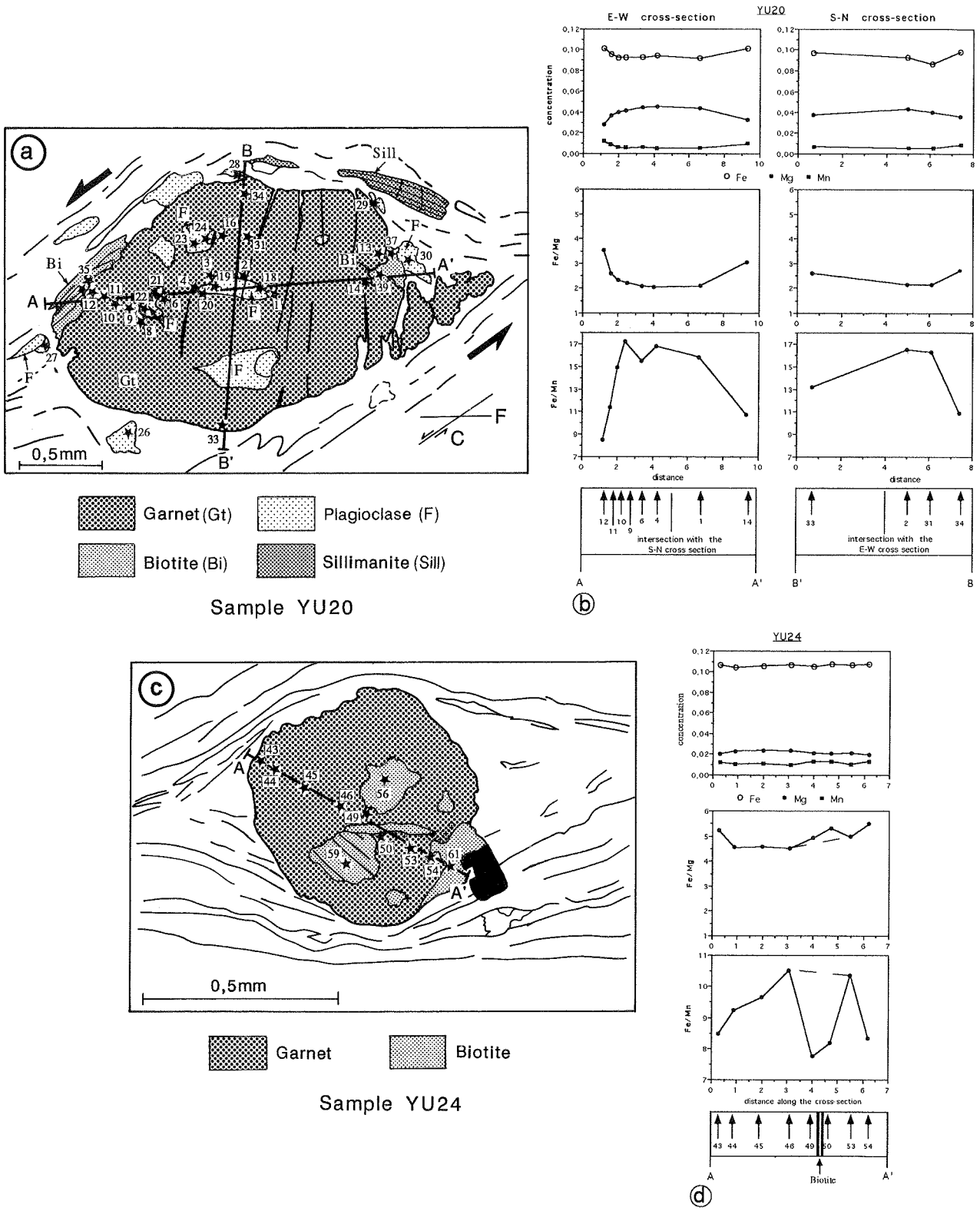

Fig. 7. Location of electron microprobe measurements in samples YU20 and YU24 (location in Fig. 4). Each star indicates the location of one microprobe measurement. (a) YU20 garnet. A–A′ and B–B′ are the 'cross sections' indicated in Fig. 9b. (b) Variation in Mn, Mg and Fe content and in Fe/Mg and Fe/Mn ratios along the 'cross sections' A–A′ and B–B′. (c) YU24 garnet. Same legend as (a). (d) Variation in Mn, Mg and Fe content and in Fe/Mg and Fe/Mn ratios along the 'cross section' A–A′. Dashed lines indicate the assumed chemical composition at points 49 and 50 in the absence of chemical re-equilibration in the vicinity of the biotite during P1b (see text).

plagioclase–garnet barometer [27] and the biotite–garnet thermometer [25].

For P1a, the geobarometric estimates are from sample YU20 and are separated by a maximum of 2.6 kbar (lines *f* and *c*, Fig. 8a). The temperature estimates are from sample YU24 and vary by 90°C (lines *A* and *B*, Fig. 8a). If we assume that samples YU20 and YU24, which are separated by 16 km along strike (Fig. 4), have recorded the same *PT* conditions during P1a, we can estimate these conditions at between 620 and 690°C and 3.5 and 6.5 kbar (660° ± 45°C and 5 ± 1.5 kbar) (Fig. 8). The assumption that samples YU20 and YU24 have recorded the same *PT* conditions seems to be quite reasonable (see below), but this *PT* estimate is not very precise as the biotites used to calculate the geothermometer seem to have undergone a partial chemical re-equilibration during P1b. This would imply that the original equilibrium between biotite and garnet corresponds to even lower temperatures and consequently lower pressures (a temperature overestimate of 100°C induces a pressure overestimate of ≈ 1.5 kbar). However, this *PT* overestimate cannot be very large as temperatures significantly lower than 660°C would imply stability of staurolite instead of garnet (R2 in Fig. 9) [28].

For P1b, all the measurements including those from sample YU24 cluster together within 2 kbar (lines *1* and *3*) and 110°C (lines *II* and *IV*) (Fig. 8b). This seems to indicate that samples YU20 and YU24 have recorded approximately the same *PT* conditions. Intersections of geobarometer and geothermometer for the same garnet points (garnets 12, 13 and 14 in sample YU20) indicate pressures ranging from 3.1 to 5.1 kbar and temperatures ranging from 680°C to 770°C (Fig. 8b). These values are confirmed by the overall geobarometer and geothermometer intersection, including those deduced from measurement on the sample YU24, which gives temperatures between 650 and 780°C and pressures between 2.7 and 6.2 kbar (Fig. 8b). P1b corresponds to *PT* conditions of approximately 710° ± 70°C and 4.5 ± 1.5 kbar.

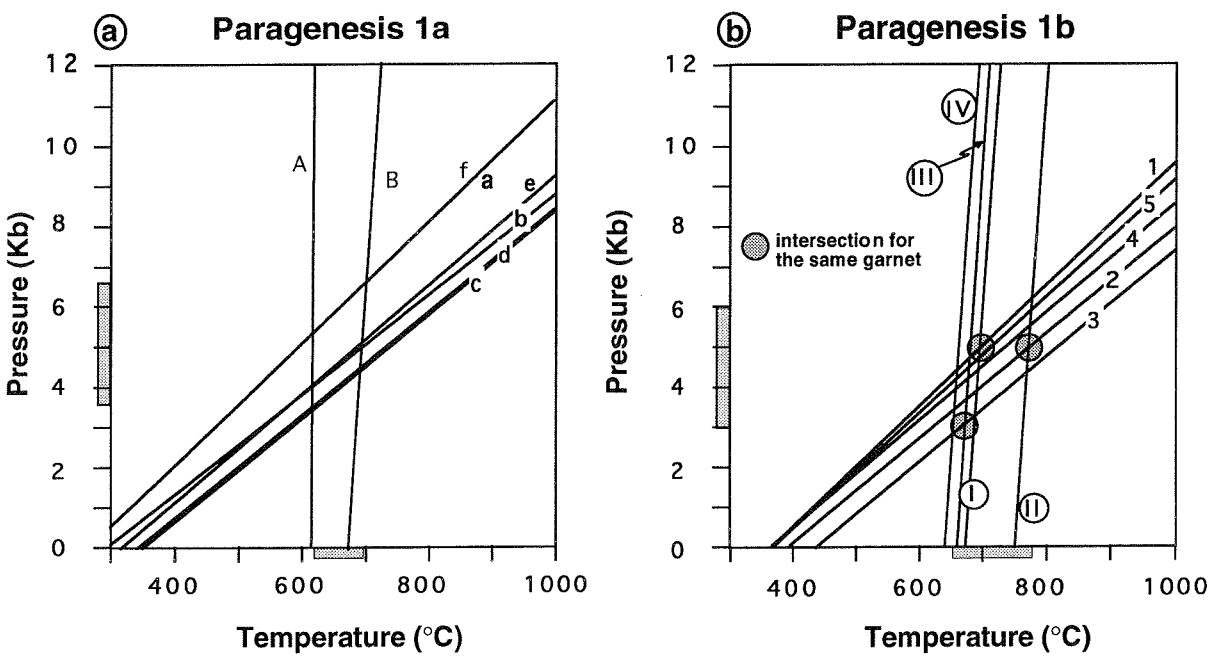

Fig. 8. Geothermometer and geobarometer estimates for (a) P1a and (b) P1b. Calculations were performed using the following data pairs (see Fig. 6): **Garnet–plagioclase barometer** [27] **for P1a** (garnet core), sample YU20: *a* = Gt1–Pl18; *b* = Gt3–Pl19; *c* = Gt4–Pl20; *d* = Gt6–Pl21; *e* = Gt8–Pl22; *f* = Gt16–Pl23 and 24. **Garnet–biotite thermometer** [25] **for P1a** (garnet core), sample YU24: *A* = Gt53–Bi59; *B* = Gt46–Bi56. **Garnet–plagioclase barometer** [27] **for P1b** (garnet rims), sample YU20: *1* = Gt12–Pl27; *2* = Gt13–Pl29; *3* = Gt14–Pl30; *4* = Gt34–Pl28; *5* = Gt33–Pl26. **Garnet–biotite thermometer** [25] **for P1b** (garnet rims), sample YU20: *I* = Gt12–Bi35; *II* = Gt13–Bi37; *III* = Gt14–Bi39; *IV* = Gt54–Bi61 (sample YU24).

Use of the Holland and Powell dataset [29] does not significantly change these results, giving, for example, 4.7 ± 0.6 kbar at 700°C for P1b. Furthermore, these *PT* calculations are in good agreement with the stability domains of the minerals of paragenesis P1 (Fig. 9) [28,30]. We conclude that conditions recorded in garnet cores (P1a) are of the order of 650°C and 5 kbar, and of the order of 710 ± 70°C and 4.5 ± 1.5 kbar for garnet rims (P1b). Garnet chemical zoning indicates an increase in temperature and a decrease in pressure between garnet cores and rims but

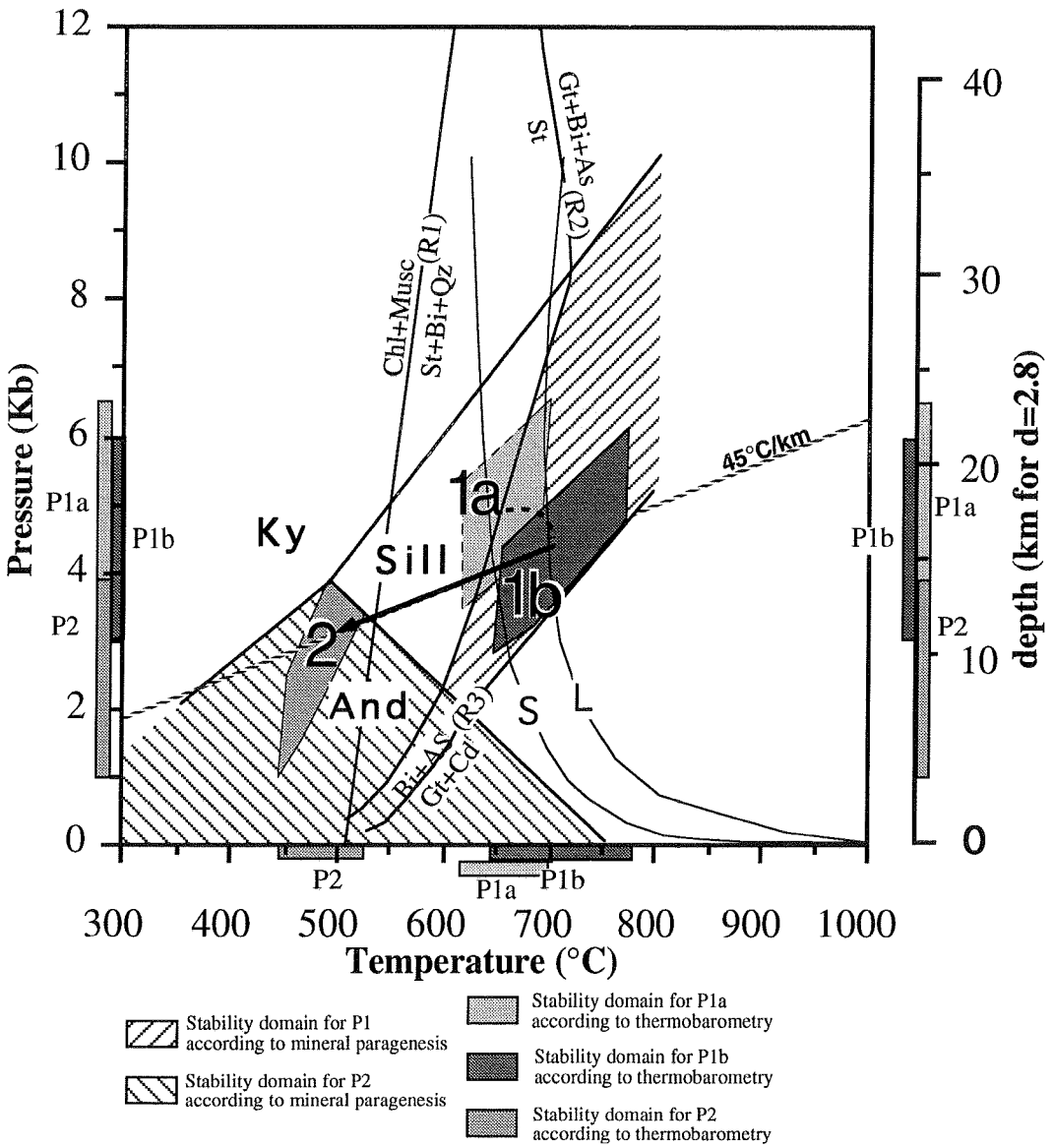

Fig. 9. Petrogenetic grid and thermobarometry estimates for P1a, P1b and P2. *Ky* = kyanite; *And* = andalusite; *Sill* = sillimanite; *As* = aluminosilicates; *Chl* = chlorite; *Musc* = muscovite; *St* = staurolite; *Bi* = biotite; *Qz* = quartz. Stability domains of sillimanite, andalusite and kyanite from [28], R1 from [30], R2 and R3 from [28]. Thermobarometry estimates from Figs 8 and 11. *L* and *S* are granitic liquidus and solidus with excess water [34]. A linear thermal gradient of 45°C/km is given for reference.

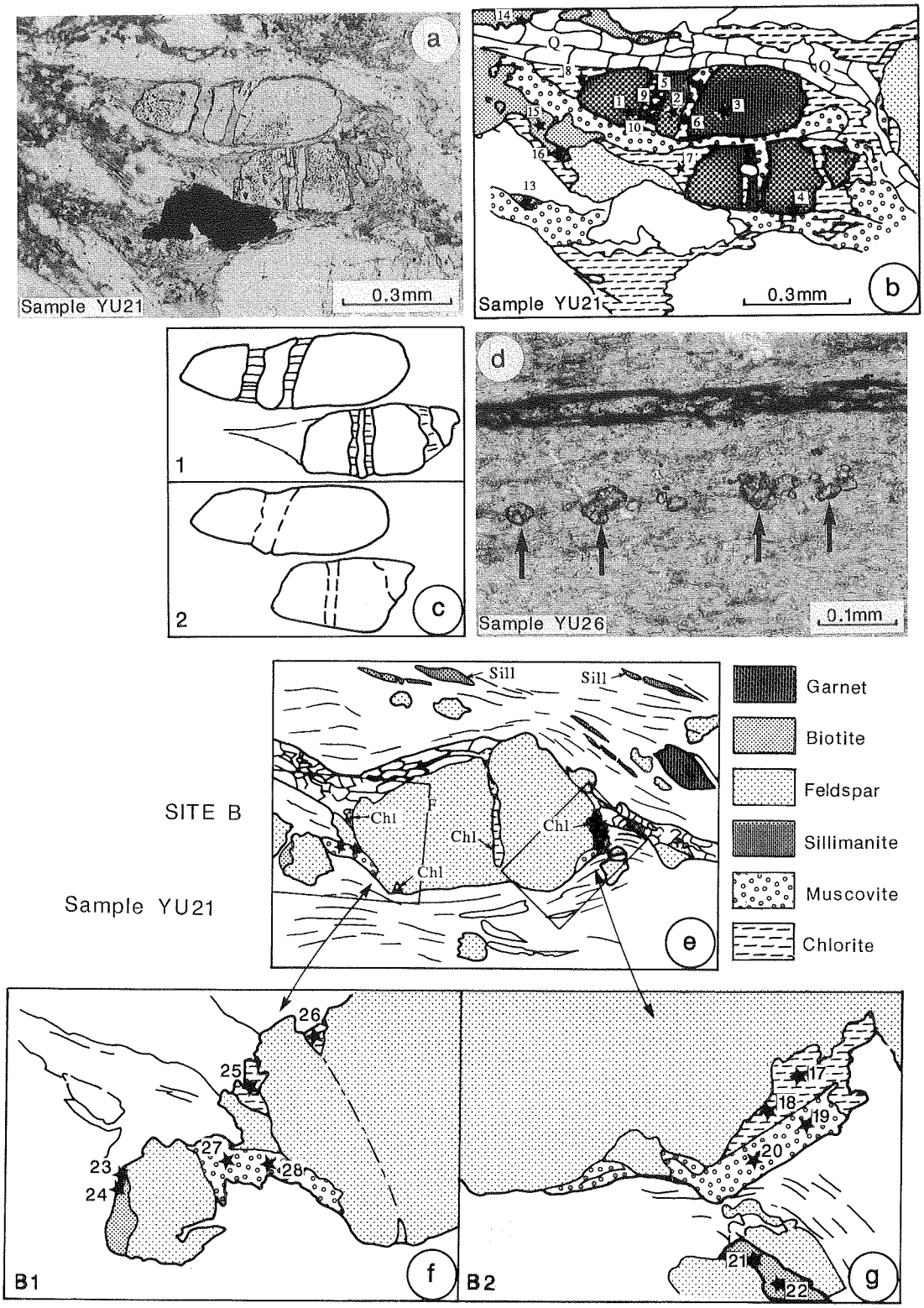

Fig. 10. Location of electron microprobe measurements in samples YU21 and YU26. (a) Microphotograph of site A in sample YU21. (b) Sketch of site A in sample YU21, each star indicating the location of one microprobe measurement. (c) Restoration of the shape of boudinaged garnets shown in (a) and (b): *1* = final shape; *2* = shape before boudinage. The garnet is stretched parallel to the mineral lineation and P2 minerals grow in gaps. (d) Microphotograph of YU26 thin section. Small grains correspond to the stretched garnets that have been analyzed. (e) Location of electron microprobe measurements in site B of sample YU21. (f and g) General sketch and details of site B (B1 and B2). Each star indicates the location of one microprobe measurement.

uncertainties in the *PT* estimates corresponding to P1a and P1b preclude precise determination of these variations.

4.2 *Estimate of the pressure–temperature conditions of the retrograde paragenesis (P2)*

Minerals corresponding to the low-grade paragenesis (or P2) are found in pressure shadows adjacent to or in cracks within porphyroclasts of the high-grade paragenesis (Fig. 5a and 10). For example, in sample YU21 (location in Fig. 4) garnets of the high-grade paragenesis with a composition comparable to those of the garnets in sample YU20 and YU24 (Fig. 6) are stretched, and in cracks between the boudins chlorite and muscovite start to grow (Fig. 10). In the matrix both chlorite and muscovite are in contact with biotite. The same association of retrograde minerals can be found in pressure shadows at the extremities of feldspar porphyroblasts (Fig. 10a). To estimate the pressure–temperature condition of paragenesis 2 we compute the biotite–muscovite–chlorite thermobarometer [31,32] in three different sites of sample YU21 (Fig. 10). Calculated log K values [32] are 4.004 (site A), 4.1124 (site B1) and 4.4202 (site B2), yielding similar curves in *PT* space (Fig. 11).

In some places the whole rock is retrograded and the high-grade paragenesis is nearly obliter-

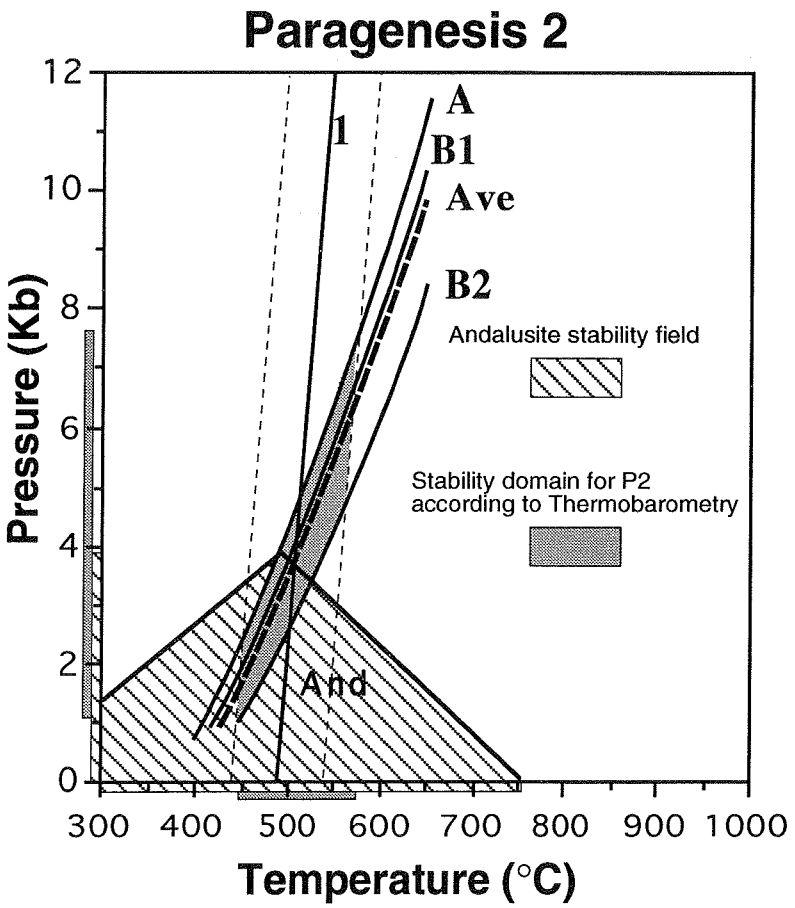

Fig. 11. P2 thermobarometry estimate. *1* = YU26 garnet–phengite thermometer for pelites poor in Ca and Mg [33]. **Muscovite–chlorite–biotite thermobarometer** [32] **on sample YU21**: *A* = average of muscovite 9,10,11,12–biotite 13,14,15,16–chlorite 5,6,7,8 (Fig. 10b); *B1* = muscovite 19,20–biotite 21,22–chlorite 17,18 (Fig. 10f); *B2* = muscovite 27,28–biotite 23,24–chlorite 25,26 (Fig 10g); *Ave* = general average. The stability domain for P2 according to thermobarometry measurement indicated corresponds to an error of ±50°C on the thermometer (small dashed lines). The actual stability domain is assumed to correspond to the part of this domain where andalusite is stable.

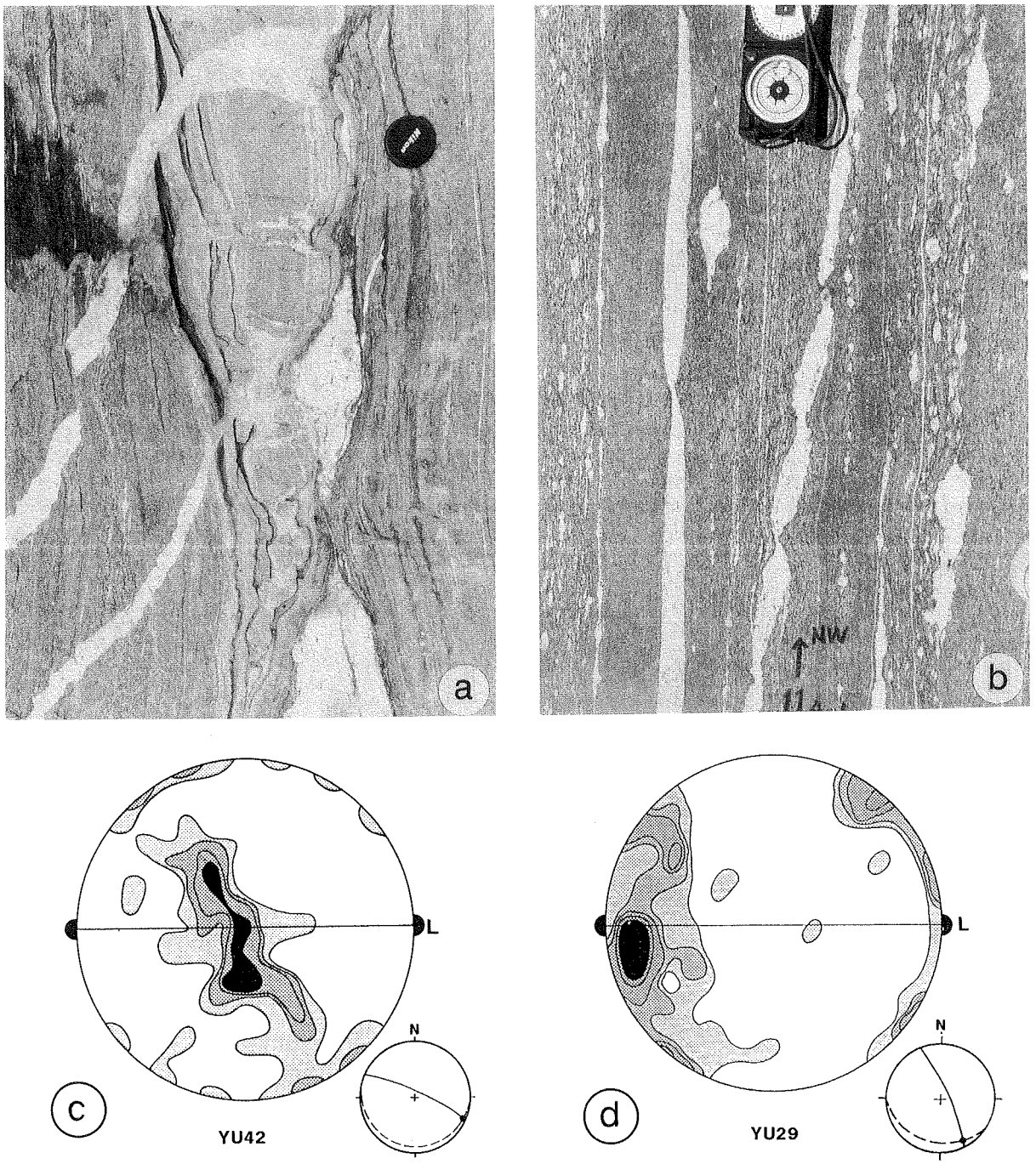

Fig. 12. Indications of high-temperature left-lateral strike-slip deformation. Site B1 (location in Fig. 2b). (a) Leucocratic layers affected by left-lateral shear and leucocratic melt filling gaps between schistosity boudins. (b) Leucocratic layers affected by left-lateral shear. (c and d) Examples of *c*-axis orientation fabrics in the Ailao Shan gneisses suggesting high-temperature left-lateral deformation: (c) shows evidence of activation of the $< a >$ prismatic glide; (d) suggests the activation of the $< c >$ prismatic glide.

ated. YU26 (location in Fig. 2) is a sample of this type of mylonite. The crystals are very small and sillimanite is retrograded to andalusite. The foliation is marked by biotite and phengite, with small garnets stretched in the direction of the lineation (Fig. 10). These garnets are probably in equilibrium with phengite in the foliation and are very rich in Mn (Fig. 6), suggesting low-grade conditions. We applied the garnet–phengite thermometer [33] to nine measurements on garnets and one in phengite to estimate the temperature corresponding to the formation of these garnets. Measurements on phengite were very difficult to perform due to the very small size of the grains, although the resulting temperature is estimated to be about 500°C (Fig. 11). If we assume that P2 of YU21 formed under the same conditions as the low-grade paragenesis of YU26, a pressure lower than 3.8 kbar in order to be consistent with the andalusite stability field is implied (Fig 11). We thus estimate the *PT* conditions of P2 at ≈ 500°C and < 3.8 kbar (or between 1 and 3.8 kbar if there is a ± 50°C uncertainty in the thermometer) (Fig. 11). It is important to note that the estimates of these *PT* conditions are far less reliable than those of P1b: (a) The angle between the two thermobarometers used is very small and, the resulting uncertainty is high (Fig 11), (b) some errors can result from the use of the garnet–phengite geothermometer [33] with Mn-rich garnets (spessartite), and (c) the two samples used are located on opposite sides of the shear zone, one side of which possibly having undergone more denudation than the other [20].

5. PTt path of the Ailao Shan mylonites during left-lateral deformation

The *PT* path of the Ailao Shan gneisses corresponding to the results presented above may be subdivided into two main stages that both take place during left-lateral shear: a prograde metamorphism (between P1a and P1b) and a retrograde evolution (from P1b to P2) (Fig. 9). The first stage, which corresponds to garnet development, starts at a temperature of the order of 550°C at a depth of ≈ 18 km (we assume a crust density of 2.8) and ends at depths of 16 ± 5 km and temperatures very close to the granitic solidus (710 ± 70 °C) (Fig. 9). Numerous qualitative observations confirm that high temperatures were reached during the left-lateral deformation. Gneisses exhibit numerous leucocratic layers parallel to the mylonitic foliation that are affected by left-lateral shear. In some outcrops, these leucocratic melts can be found filling gaps between boudins formed during left-lateral deformation (Fig. 12a). At site B1 (Fig. 2), a detailed study shows that several generations of leucocratic veins where progressively intruded and deformed during the left-lateral deformation (Fig. 12b) [4]. These observations indicate that the leucocratic melt emplacement was coeval with left-lateral deformation [4]. The occurrence of migmatitic rocks (Fig. 2) and the small scale of some of the leucocratic layers (< 10 cm wide) suggests that the melted (or partially melted) source of these layers is not far beneath the present-day outcrop. This would imply that temperatures of at least 600°C [34] were reached in the shear zone during the left-lateral movement.

A second line of evidence for high-temperature left-lateral deformation is given by quartz *c*-axis preferred orientations in the mylonites. All of these fabrics are compatible with a left-lateral asymmetric deformation but correspond to activation of different glide systems that are characteristic of different temperatures [4]. Many of these fabrics indicate the activation of the $\langle a \rangle$ prismatic glide (Fig. 12c), which is active at temperatures of more than 500°C [35]. The quartz *c*-axis preferred orientation of sample YU29 (location in Fig. 2) showing a maxima close to the lineation (Fig. 12e) is interpreted to correspond to the activation of the $\langle C \rangle$ prismatic glide [4], which is active in conditions close to the granitic solidus [36,37]. Despite uncertainties it seems that substantial heating (> 50°C) occurred in the Ailao Shan during the left-lateral deformation between P1a and P1b, leading to temperatures compatible with crustal partial melting. Corresponding uplift seems moderate (≈ 2 km). This episode necessarily predates 23 Ma, which is the crystallization age of monazite and xenotime in the leucocratic layers of the northeast Ailao Shan [2].

No indication of mantle-derived rocks has been found within the gneissose shear zone and the total recorded uplift of the Ailao Shan gneisses (from P1a to present) is ≈ 18 km (Fig. 9). The lack of a good pressure estimate for P2 makes it

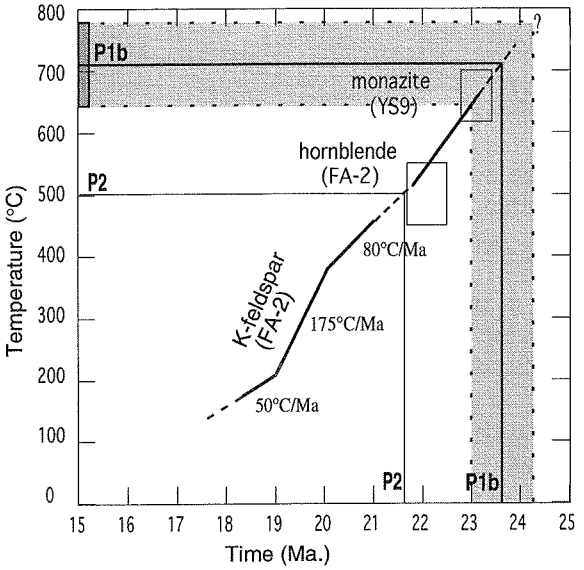

Fig. 13. Thermal history of the eastern border of the Ailao Shan shear zone north of Mosha. U-Pb age on monazite of sample YS9 (site E6, Fig. 5) from [2]. $^{40}Ar/^{39}Ar$ data (amphibole and cooling history of K-feldspars) of sample FA-2 (site E5, Fig. 5) are from [20].

difficult to estimate relative amounts of uplift during the left-lateral deformation and after the initiation of the still active Range Front fault bounding the massif. According to our thermobarometric results, uplift coeval with left-lateral deformation (until P2) could range from $\approx$ 15 km to negligible (Fig. 9). Cooling corresponding to the P1b–P2 transition is better constrained and is estimated at 200°C. A thermochronological study based on samples YS9 (site E6, Fig. 4) [2] and FA-2 (site E5, Fig. 4) [20] constrains the cooling ages of the northeast Ailao Shan gneisses: temperatures corresponding to P1b and P2 were reached at $\approx$ 23.5 and 21.5 Ma respectively (Fig. 13). The short duration of the transition from P1b to P2 ($\approx$ 2 Ma) may be the reason for staurolite not being observed. According to the same study, rapid cooling lasted until 19 Ma (Fig. 13) [20]. At this time, in accordance with the opening kinematics of the South China Sea, left-lateral shear was active along the Red River fault zone and lasted until 17 Ma [19]. This rapid cooling coeval with left-lateral deformation favours the hypothesis of a significant uplift at this time [20].

These results raise two fundamental questions concerning metamorphism in strike-slip shear zones: (1) which mechanism explains uplift, and (2) how can we explain these very high temperatures that occur during deformation? We shall assess these two questions separately.

6. Discussion

6.1 Uplift during left-lateral shear

The occurrence of vertical movement in a strike-slip zone implies an oblique vector movement that can be divided into two components, a large purely strike-slip component, and a small purely normal or reverse component that is responsible for the uplift.

A left-lateral movement on a plane dipping toward the northeast, along a line with a small pitch toward the southeast, implies a small thrust component. Taking into account the fact that the horizontal offset is very large (more than 500 km of the total offset [e.g., 3,4]), a significant uplift may be obtained with a very small pitch. For example, on a plane dipping 65° toward the northeast (the average foliation in this part of the Ailao Shan massif does indeed dip 65° toward the northeast; Fig. 2), a 5 km vertical component of movement may be explained by a pitch of only 4° toward the southeast for 100 km of horizontal displacement. We do not know the extent of the horizontal displacement along the Ailao Shan shear zone between P1b and P2 and it is thus impossible to calculate the corresponding pitch. However, using the fault kinematics deduced from the opening of the South China Sea [19] in the time interval 23.5–21.5 Ma (ages of P1b and P2 deduced from the thermal history of the gneiss), the horizontal offset may be estimated at 55 km (horizontal rate $\approx$ 2.75 cm/yr at this time). For an offset of 55 km, a pitch of only 7° is necessary to account for a vertical movement of 5 km. Due to the uncertainties in the thermal history, thermobarometers and fault kinematics this estimate is only approximate, but it is consistent with the observation that the lineation has a pitch of 0–20° to the southwest in the sampling area. Lineation pitches may easily explain a limited uplift between P1b and P2 and/or P1a and P1b. The existence of a reverse component of movement may also explain the contact between high-grade gneisses and lower grade schists along the Ailao Shan fault (Fig. 2).

Alternatively, uplift in the shear zone may also result from a normal component of movement along the fault. This hypothesis is suggested by the kinematics of the RRFZ deduced from the South China Sea opening kinematics, the RRFZ kinematics implying a component of compression along the fault approximately north of the northern tip of the Ailao Shan massif and an extension component south of this point [19]. A component of normal faulting also provides a more efficient mechanism for the rapid cooling of the gneisses between 21 and 19 Ma [20]. No obvious structural features capable of accounting for this normal component of movement have yet been found in the Ailao Shan massif. Traces of the normal fault (or left-lateral/normal fault) may have since been eroded. These two causes of uplift (normal and reverse component of movement) are not incompatible as they may have existed at different times in the same area or at different places along strike at the same time.

6.2 High-temperature deformation

In continental areas that have not experienced recent tectonism the crust is much cooler than the temperature estimates provided in this study. For example, in the Canadian shield temperatures corresponding to P2 (500°C) and P1b (710°C) are thought to be reached below 40 km and 100 km respectively [38]. In the case of the RRFZ such temperatures corresponded to much shallower depths ($\leqslant$ 13 km for P2 and 16 ± 5 km for P1b). This strongly suggests a perturbed geotherm along the strike-slip fault at the time of left-lateral shearing, and raises questions regarding the heat source. High temperatures seem to be restricted to the shear zone itself, as no Tertiary metamorphic or magmatic rocks are visible northeast or souhwest of it [9] (Fig. 1). These observations strongly suggest a mechanism that is capable of creating heat in the shear zone itself and/or of efficiently transfering heat from below within the shear zone.

Heat production within the continental crust is essentially due to radioactivity, and large-scale thickening of the radioelement-rich crust is an efficient mechanism by which high geothermal gradients can be produced [e.g., 39]. However, in the case of the Ailao Shan, crustal thickening seems to be moderate and would not therefore explain the observed heat localization within the shear zone. Shear heating is a more appealing mechanism, as it may explain the localization of metamorphism—thermal metamorphic intensity decreases away from the centre of the shear zone. In this hypothesis the high-grade gneisses correspond to the zone of maximum deformation where heat is produced by shear heating. The greenschists that bound the gneisses to the southwest could be the result of the same metamorphism that produced the gneisses, but at a lower temperature because they are farther from the zone of maximum deformation. However, despite being long advocated, the role of shear heating has encountered some controversy: As the rocks increase in temperature, they soften and progressively decrease their frictional heat production. Consequently, shear heating is not believed to be an efficient mechanism for reaching very high temperatures in a homogeneous medium [e.g., 40,41]. This indicates that some of the heat must come from below, probably advected by magmas and/or fluids in the shear zone.

This hypothesis is strongly supported by the observation that emplacement of granitic bodies occurred during the left-lateral deformation. Extension is an efficient mechanism in causing uplift and heat advection, as for example in continental rifts. In the case of Yunnan, Miocene uplift is localized in the RRFZ and limited to a maximum of $\approx$ 20 km. This local uplift may have produced local crustal partial melting and facilitated heat advection within the shear zone. This is supported by the fact that granitic bodies become more numerous and larger within the shear zone toward the southeast [9], where the extension component along the RRFZ predicted by the opening kinematics of the South China Sea is larger [19]. On the other hand, most of the recorded uplift post-dates the thermal peak (P1b), suggesting that high temperatures are not a consequence of uplift but rather a cause of it. Fleitout and Froidevaux [41] proposed that shear heating in a multi-layered medium may produce partial melting, the competent layer being able to produce heat even at very high temperatures and inducing the melting of the softer layers. If the fault affects the Moho and is rooted at the base of the lithosphere, as is suggested by the large

amount of offset [e.g., 4,5] and the opening of the South China Sea at its southeasterly termination [19], heat produced by shear heating in the upper mantle may have heated the crust through conduction [1]. The time necessary for such heat transfer would be of the order of 14 Ma, assuming $\kappa = 7 \times 10^{-7}$ [42] and a crustal thickness of 35 km.

To test this hypothesis, we conducted a steady-state numerical simulation of a two-layer medium affected by a strike-slip fault (Fig. 14) [43]. The model comprises a 35 km thick granitic layer representing the crust and a 65 km thick dunite layer representing the upper mantle. These layers are affected by a strike-slip fault with a displacement of 3.3 cm/yr (the average rate assumed on the RRFZ between 28 and 17 Ma [19]). The temperature is fixed at 20°C at the top of the model and at 1000°C at its base. This latter temperature is higher than temperature estimates at this depth for old continental areas [e.g., 38] but may be justified because Yunnan experienced a limited Cenozoic shortening and the radioactive heat generation within the crust is not taken into account in our model. Shear stresses on the fault corresponding both to brittle fracture [44] and ductile deformation [e.g., 45] are calculated along the fault as a function of depth and temperature. The power flow laws of the crust and the mantle are those of wet granite [46] and wet dunite [47] respectively. At a given depth, the deformation mechanism is assumed to be that for which the corresponding shear stress τ is the lowest. The corresponding heat production is calculated. The heat transfer is only conductive. Thermal steady state in the crust should be reached after ≈ 15 Ma, as the main heat sources are located at the brittle/ductile transition within crust and just below the Moho. Temperatures of ≈ 400 and 750°C are reached at the 20 km depth and at the base of the crust respectively (Fig. 14). The corresponding temperature increases are ≈ 180 and 400°C with respect to the initial linear temperature gradient from the base to the top (Fig. 14). The temperature at 20 km is significantly lower than estimates of P1b. However, temperatures at the base of the crust are higher than the liquidus of rocks of granitic composition at the 35 km depth (10 kbar) if such rocks contain more than ≈ 8 wt% water [34]. According to this model, shear heating in the mantle may explain a significant temperature increase in the lower crust sufficient to produce partial melting. Limited uplift, most probably due to an extension component

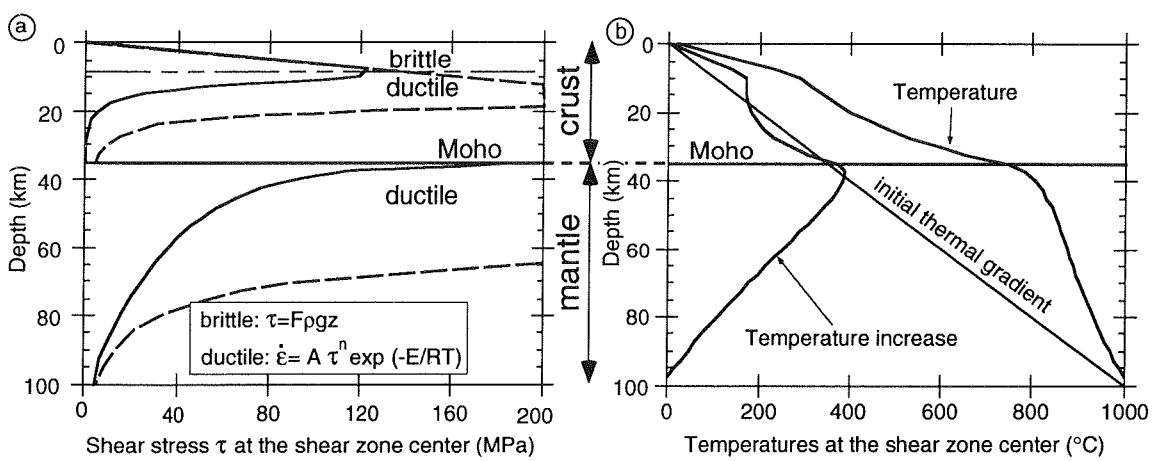

Fig. 14. Steady-state numerical model of shear heating on a lithospheric strike-slip fault. (a) Strength profile of the lithosphere along the fault as a function of depth. Dashed lines correspond to the strength profile for the same parameters but without any shear heating. (b) Temperature and temperature increase due to shear heating in the shear zone, with respect to the initial regular thermal gradient along the fault. Parameters for this model are $V = 3.3$ cm/year, thermal conductivity = 2.5 W m^{-1} K^{-1}, and $F = 0.6$ [44]. *Crust* = wet westerly granite: $A = 2 \times 10^{-4}$ MPa^{n}s^{-1}, $n = 1.9$, $E = 1.4 \times 10^5$ J/mol [46], $\rho = 2.8$. *Mantle* = Aheim dunite: $A = 3.98 \times 10^2$ MPa^{n}s^{-1}, $n = 4.5$, $E = 4.98 \times 10^5$ J/mol [47], $\rho = 3.2$.

along the strike-slip fault, may have facilitated magma and hot fluid advection to an extent sufficient to transfer this heat anomaly to the middle crust.

7. Conclusion

The petrology of the Ailao Shan massif, the largest metamorphic core of the Ailao Shan–Red River shear zone, indicates that during the left-lateral deformation gneisses in the shear zone experienced a prograde metamorphism from conditions of the order of 5 kbar and 650°C (P1a) to conditions close to the granitic solidus (P1b, 4.5 $\pm$ 1.5 kbar and 710 $\pm$ 70°C). Emplacement of some leucocratic melts, probably resulting from crustal partial melting occurred at $\approx$ 23 Ma within the shear zone. Gneisses were retrograded in the greenschist facies (P2, $<$ 3.8 kbar and $\approx$ 500°C) before the end of left-lateral shearing. This rapid cooling was probably due to a normal component of movement on the left-lateral fault. Shear heating is an appealing mechanism for explaining very high temperature deformation in the strike-slip shear zone and the strong horizontal metamorphic gradient on either side of it. If shear heating is limited to the crust it does not produce very high temperatures. However, a simple numerical model of strike-slip faulting affecting the whole lithosphere suggests that shear heating in the mantle may produce temperatures that are sufficiently high to partially melt the lower crust. Advection in the shear zone of magmas and/or fluids that originated at the base of the crust may have transfered a large amount of this heat to the middle and upper crust. The schists associated with ultramafic rocks, bounding the mylonitic gneisses, previously interpreted as resulting from a collision related metamorphism, may instead be of medium pressure and temperature resulting from a 'contact' metamorphism of the shear zone at middle crust depths. If shear heating is capable of producing partial melting in the lower crust it could partly explain strain localization in the continental lithosphere, especially in large strike-slip fault zones. This would imply the existence of a special metamorphism associated with large-scale continental strike-slip faulting and an alternative mechanism for continental magmas generation. However, more precise geochemical studies on the syntectonic granites and fluid circulation in the Ailao Shan and other large ductile strike-slip shear zones are needed to test this hypothesis.

Acknowledgements

We acknowledge P. Tapponnier and R. Lacassin for help in the field, T.M. Harrison, Jeff Fillipone and M. Korn for helpful discussion, G. Aveline and E. Lesur for drafting, and Y. Ricard and P. Bird for help on the numerical model. P. Bertrand and C. Jaupart are thanked for helpful reviews.

References

1 P. Tapponnier, R. Lacassin, P.H. Leloup, U. Schärer, Zhong Dalai, Wu Haiwei, Liu Xiaohan, Ji Shaocheng, Zhang Liangshen and Zhong Jiayou, The Ailao Shan–Red River metamorphic belt: Tertiary left lateral shear between Sundaland and South China, Nature 343, 431–437, 1990.

2 U. Schärer, P. Tapponnier, R. Lacassin, P.H. Leloup, Zhong Dalai and Ji Shaocheng, Intraplate tectonics in Asia: a precise age for large-scale Miocene movement along the Ailao Shan–Red River fault zone, China, Earth Planet. Sci. Lett. 97, 65–77, 1990.

3 P.H. Leloup, R. Lacassin, P. Tapponnier, H. Maluski, J.R. Kienast, Zhong Dalai, Liu Xiaohan, Zhang Liangshen and Zhong Jiayou, New evidence for Miocene left-lateral movement along the Red River shear zone (Yunnan, China), EOS 71, 1617–1618, 1990.

4 P.H. Leloup, Cinématique des déformations 'himalayennes' dans la zone de cisaillement crustale de l'Ailao Shan–Fleuve Rouge, Ph.D. Thesis, Univ. Paris 6, 1991.

5 R. Lacassin, P.H. Leloup and P. Tapponnier, Bounds on strain in large Tertiary shear-zones of SE Asia from boudinage restoration, J. Struct. Geol., in press.

6 Huang Chi Ching (T.K.), An outline of the tectonic characteristics of China, Eclogae Geol. Helv. 71(3), 611–635, 1978.

7 P. Tapponnier and P. Molnar, Active faulting and tectonics in China, J. Geophys. Res. 82, 2905–2930, 1977.

8 C.R. Allen, A.R. Gillespie, Y. Han, K.E. Sieh, B. Zhang and C. Zhu, Red River and associated faults, Yunnan province, China: Quaternary geology, slip rates, and seismic hazard, Geol. Soc. Am. Bull. 95, 686–700, 1984.

9 Bureau of Geology and Mineral Resources of Yunnan, Geological map of Yunnan, scale 1:1000000, 1983.

10 Liu Changshi, Zhu Jinchu, Chu Xuejun, Xu Xisheng, Cai Dekun and Yang Pin, The Hercynian–Indosinian collision type granites of west Yunnan and their tectonic significance, J. Southeast Asian Earth Sci. 3(1–4), 263–270, 1989.

11 Yan Qizhong, Zhang Guoking, Kan Rongju and Hu Hongxiang, the crust structure of the Simao to Malong profile, Yunnan province, China, J. Seismol. Res. 8(2), 249–264, 1985.

12 Duan Xinhua and Zhao Hong, The Ailao Shan–Tengtiohe fracture: the subduction zone of an ancient plate, Acta Geol. Sin. 55(4), 258–266, 1981.
13 Lu Liangzhao, The metamorphic series and crustal evolution of the basement of the Yangtze Platform, J. Southeast Asian Earth Sci. 3(1–4), 293–301, 1989.
14 Fan Chengjing, The tectonic–metamorphic belt of Mt. Ailao in Yunnan province, Geol. Yunnan 5, 281–291, 1986.
15 A.W. Bally, C.R. Allen, R.B. Geyer, W.B. Hamilton, C.A. Hopson, P.H. Molnar, J.E. Oliver, N.D. Opdyke, G.P. Lafker and F.T. Wu, Notes on the geology of Tibet and adjacent areas: report of the American plate tectonics delegation to the People's Republic of China, U.S. Geol. Surv. Open-File Rep. 80-501, 1980.
16 A.M.C. Sengör, Tectonic subdivisions and evolution of Asia, Bull. Tech. Univ. Istanbul 40, 355–435, 1987.
17 C.S. Hutchison, The paleo-Tethyan realm and Indosinian orogenic system of southeast Asia, in: Tectonic Evolution of the Tethyan Region, A.M.C. Sengör, ed., pp. 585–643, Kluwer, 1989.
18 A. Briais, Cinématique d'ouverture de la mer de Chine du Sud (Nan Hai). Implications pour la tectonique Tertiaire de l'Asie, Ph.D. Thesis, Univ. Paris 6, 1989.
19 A. Briais, P. Patriat and P. Tapponnier, Updated interpretation of magnetic anomalies and seafloor spreading stages in the South China Sea: implications for the Tertiary tectonics of SE Asia, J. Geophys. Res., in press.
20 T.M. Harrison, Chen Wenji, P.H. Leloup, F.J. Ryerson and P. Tapponnier, An early Miocene transition in deformation regime on the Red River Fault Zone, Yunnan, and its implications for Indo-Asian tectonics, J. Geophys. Res. 97, 1992.
21 M.J. Holdaway, Stability of andalusite and the aluminum silicate phase diagram, Am. J. Sci. 271, 97–131, 1971.
22 Zhang Qi, Li Dazhou and Zhang Kuiwu, Preliminary study of paleo-Tethyan ophiolites in the Hengduan mountain region (HMR), China, J. Southeast Asian Earth Sci. 3(1–4), 249–254, 1989.
23 Zhang Ru Yuan, Cong Bo Lin and Li Yong Gang, Petrology of blueschist in western Yunnan Province, China, and its tectonic significance, Sci. China Ser. B 33(9), 1990.
24 J.M. Ferry and F.S. Spear, Experimental calibration of the partitioning of Fe and Mg between biotite and garnet, Contrib. Mineral. Petrol. 66, 113–117, 1978.
25 K.V. Hodges and F.S. Spear, Geothermometry and the Al_2SiO_5 triple point at Mt. Moosilauke, New Hampshire, Am. Mineral. 67, 1118–1134, 1982.
26 R.C. Newton and H.T. Haselton, Thermodynamics of the garnet–plagioclase–Al_2SiO_5–quartz geobarometer, in: Thermodynamics of Minerals and Melts, R.C. Newton, A. Navrotsky and B.J. Wood, eds., pp. 129–145, Springer, New York, 1981.
27 J. Ganguly and S. Saxena, Mixing properties of aluminosilicate garnets: constraints from natural and experimental data, and applications to geothermo-barometry, Am. Mineral. 69, 88–97, 1984.
28 F.S. Spear and J.T. Cheney, A petrogenetic grid for pelitic schists in the system SiO_2–Al_2O_3–FeO–MgO–K_2O–H_2O, Contrib. Mineral. Petrol. 101, 149–164, 1989.
29 T.J.B. Holland and R. Powell, An enlarged and updated internally consistent thermodynamic data set with uncertainties and correlations: the system K_2O–Na_2O–CaO–MgO–MnO–FeO–Fe_2O_3–Al_2O_3–TiO_2–SiO_2–CO_2–H_2O–O_2, J. Metamorph. Geol. 8, 89–124, 1990.
30 G. Hoschek, The stability of staurolite and chloritoid and their significance in metamorphism of pelitic rocks, Contrib. Mineral. Petrol. 22, 207–232, 1969.
31 R. Powell and J.A. Evans, A new geobarometer for the assemblage biotite–muscovite–chlorite–quartz, J. Metamorph. Geol. 1, 331–336, 1983.
32 K. Bucher-Nurminen, A re-calibration of the chlorite–biotite–muscovite geobarometer, Contrib. Mineral. Petrol. 96, 519–522, 1987.
33 T.H. Green and P.L. Hellman, Fe–Mg partitioning between coexisting garnet and phengite at high pressure, and comments on a garnet–phengite geothermometer, Lithos 15, 253–266, 1982.
34 C.R. Stern and J.W. Wyllie, Phase relationships of I-type granite with H_2O to 35 kilobars: the Dinkey lakes biotite–granite from the Sierra Nevada batholith, J. Geophys. Res. 86, 10412–10422, 1981.
35 A. Nicolas and J.P. Poirier, Crystalline Plasticity and Solid State Flow in Metamorphic Rocks, 444 pp., Wiley-Interscience, New York, 1976.
36 Ph. Blumenfeld, Evidence for dominant prismatic $<C>$ slip in quartz deformed under conditions close to the granitic solidus, Terra Cognita 5, 255, 1985 (Abstr.).
37 G. Gapais and B. Barbarin, Quartz fabric transition in a cooling syntectonic granite (Hermitage massif, France), Tectonophysics 125, 357–370, 1986.
38 C. Pinet, C. Jaupart, J.C. Mareschal, C. Gariepy, G. Bienfait and R. lapointe, Heat flow and structure of the lithosphere in the eastern Canadian shield, J. Geophys. Res. 96, 19941–19963, 1991.
39 Y. Gaudemer, C. Jaupart and P. Tapponnier, Thermal control on post-orogenic extension in collision belts, Earth Planet. Sci. Lett. 89, 48–62, 1988.
40 J.P. Brun and P. Cobbold, Strain heating and thermal softening in continental shear zones: a review, J. Struct. Geol. 2, 149–158, 1980.
41 L. Fleitout and C. Froidevaux, Thermal and mechanical evolution of shear zones, J. Struct. Geol. 2, 159–164, 1980.
42 W.B. Durham, V. Mirkovich and H.C. Heard, Thermal diffusivity of igneous rocks at elevated pressure and temperature, J. Geophys. Res. 92, 11615–11634, 1987.
43 Y. Ricard, C. Froidevaux and J.F. Hermance, Model heat flow and magnetotellurics for the San Andreas and oceanic transform faults, Ann. Geophys. 1, 47–52, 1983.
44 J.D. Byerlee, Friction of rocks, Pure Appl. Geophys. 116, 615–626, 1978.
45 N.L. Carter and M.C. Tsenn, Flow properties of continental lithosphere, Tectonophysics 136, 27–63, 1987.
46 F.D. Hansen and N.L. Carter, Semibrittle creep of dry and wet Westerly granite at 1000 MPa, 24th U.S. Symp. Rock Mechanics, pp. 429–447, Texas A&M Univ., College Station, Tex., 1983.
47 P.N. Chopra and M.S. Paterson, The experimental deformation of dunite, Tectonophysics 78, 453–473, 1981.